1-9-2017

Implications of sea ice on Southern Ocean microseisms detected by a seismic array in West Antarctica

Martin J. Pratt
Washington University in St. Louis

Douglas A. Wiens
Washington University in St. Louis

J. Paul Winberry
Central Washington University

Sridhar Anandakrishnan
Pennsylvania State University

Garrett G. Euler
Los Alamos National Laboratory

Recommended Citation

Martin J. Pratt, Douglas A. Wiens, J. Paul Winberry, Sridhar Anandakrishnan, Garrett G. Euler, Implications of sea ice on Southern Ocean microseisms detected by a seismic array in West Antarctica, Geophysical Journal International, Volume 209, Issue 1, 1 April 2017, Pages 492–507, https://doi.org/10.1093/gji/ggx007

Geophysical Journal International

Geophys. J. Int. (2017) **209,** 492–507
Advance Access publication 2017 January 9
GJI Seismology

doi: 10.1093/gji/ggx007

Implications of sea ice on Southern Ocean microseisms detected by a seismic array in West Antarctica

Martin J. Pratt,[1] Douglas A. Wiens,[1] J. Paul Winberry,[2] Sridhar Anandakrishnan[3] and Garrett G. Euler[4]

[1]*Department of Earth and Planetary Science, Washington University in St. Louis, St. Louis, MO* 31030*, USA. E-mail: martin@seismo.wustl.edu*
[2]*Department of Geological Sciences, Central Washington University, Ellensburg, WA* 98926*, USA*
[3]*Department of Geosciences, Pennsylvania State University, State College, PA* 16802*, USA*
[4]*Earth and Environmental Sciences Division, Los Alamos National Laboratory, Los Alamos, NM* 87545*, USA*

Accepted 2017 January 6. Received 2017 January 2; in original form 2016 March 22

SUMMARY

The proximity of Southern Ocean storms coupled with seasonal variation in sea ice make Antarctica ideal for the study of microseism sources. We explore frequency-dependent beamforming results using a short-duration, 60 km aperture, broad-band seismic array located on the Whillans Ice Stream, West Antarctica. Locations of single-frequency microseism (13–16 s period) generation are in regions where the continental shelf is ice-free, consistent with previous studies, and show Rayleigh wave sources remaining at consistent backazimuths throughout the duration of the array. Beamforming analysis of daily noise correlations shows that long-period double-frequency microseisms (9–11 s) consist predominantly of Rayleigh waves excited by storms in the Southern Ocean. Modelling of source locations based on wave–wave interaction provides a good fit to our data at these periods. We show that short-period double-frequency microseisms (5–7 s) in Antarctica consist of crustal phase *Lg* and body waves. *Lg* arrivals propagate through regions of continental crust and our data show that the *Lg* energy is generated when storm systems interact with the sea-ice-free continental shelf during austral summers. Ultra-short-period (0.3–2 s) microseismic body waves back project to regions that correlate with oceanic storm systems in both the Southern and Northern Hemispheres.

Key words: Interferometry; Body waves; Surface waves and free oscillations; Wave propagation; Antarctica.

1 INTRODUCTION

The seismic noise field contains continuous microseisms, which are ground oscillations generated independent of any earthquake activity. These microseisms consist of propagating seismic waves generated by interactions between the atmosphere, ocean and the solid Earth that are observed as peaks within the background seismic amplitude spectrum predominantly between 3 and 30 s period. It is generally understood that these microseisms are sourced from ocean gravity waves (Longuet-Higgins 1950; Hasselmann 1963). Noise spectra show two peaks at ∼14 and 5–7 s referred to as single-frequency (SF, or primary) and double-frequency (DF, or secondary) microseisms respectively (Hasselmann 1963; Haubrich *et al*. 1963; Bromirski & Duennebier 2002; Ardhuin *et al*. 2011, 2012). Microseisms are mainly characterized by surface waves including both Rayleigh and Love waves (Haubrich *et al*. 1963). While the relative amplitude between the SF and DF peaks varies, microseisms are almost always dominated by DF surface waves. Relatively smaller amplitude body wave microseisms have also been observed (Backus *et al*. 1964; Haubrich & McCamy 1969; Vinnik 1973; Gerstoft *et al*. 2006a) including core phases (Gerstoft *et al*. 2008; Koper *et al*. 2009, 2010; Landès *et al*. 2010). DF microseism body waves have been detected using seismic arrays (Koper *et al*. 2009, 2010; Obrebski *et al*. 2013; Euler *et al*. 2014), and appear to originate from the centre of storms over the deep ocean where wind speeds are highest. Zhang *et al*. (2010) also noted that the propagation speed of the storm may cause the source location of DF body waves to be located further behind the storm centre, and the proximity of landmasses and islands may also reflect energy and shift the DF source to more coastal facing locations.

SF microseism source locations have been inferred to be coastal, continental shelf sites (Cessaro 1994). These waves are generated at the same frequency as ocean gravity waves and are thought to be due to the interaction of shoaling ocean swells causing pressure fluctuations on the continental shelf (Hasselmann 1963; Cessaro 1994). DF surface wave microseisms, at twice the frequency of ocean gravity waves, have also been inferred to be created by coastal interactions (Bromirski *et al*. 2005, 2013; Bromirski & Gerstoft 2009), although recent surface and body wave studies have also provided evidence for an open ocean source (e.g. Kedar *et al*. 2008; Beucler *et al*.

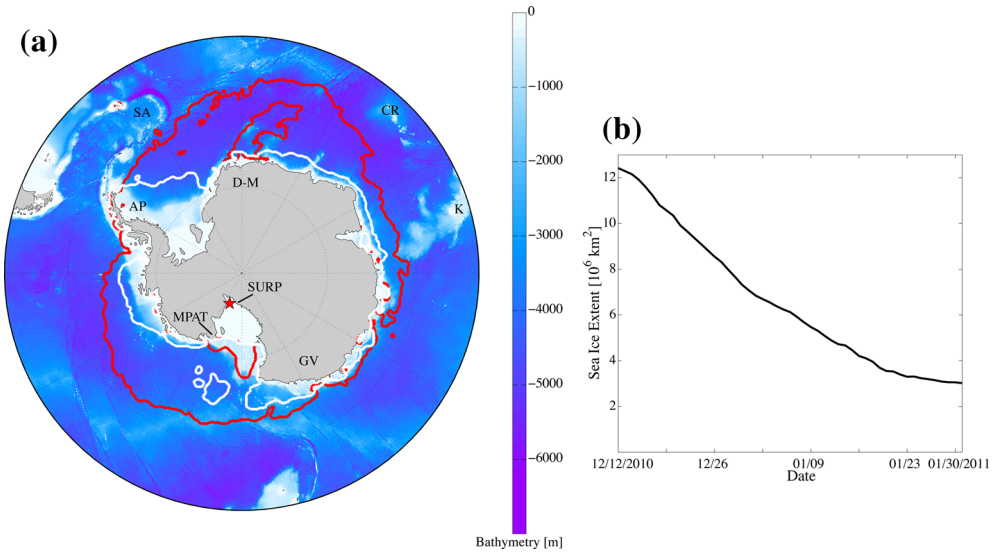

Figure 1. (a) Southern Ocean bathymetry from ETOPO1 (Amante & Eakins 2009) and sea ice extent. Red contour shows the sea ice extent for 2010 December 1 while the white contour corresponds to 2011 January 31 (Cavalieri *et al*. 1996, updated yearly). Geographic regions of interest to this study are marked with the following acronyms—AP: Antarctic Peninsula; CR: Conrad Rise; D-M: Dronning-Maude Land; GV: George V Land; K: Kerguelen Plateau; SA: Scotia Arc. The WIS seismic array location is marked by the red star, and the locations of the POLENET/ANET stations SURP & MPAT are indicated. (b) Sea ice extent as a function of time for a typical year during the dates of the WIS Array deployment (Cavalieri *et al*. 1996, updated yearly).

2015). DF microseism generation theory uses the interaction of two gravity waves travelling in opposite directions. This interaction creates standing waves on the ocean surface that cause pressure fluctuations at twice the ocean wave frequency, exciting mainly *P* and *SV* seismic waves in the solid Earth (Hasselmann 1963; Kedar *et al*. 2008; Kedar 2011). The resulting surface waves are dominantly Rayleigh waves (Gualtieri *et al*. 2013). Longuet-Higgins (1950) showed that this type of excitation is heavily influenced by bathymetry and proposed that long-period DF microseisms are mainly excited at deeper ocean depths (although a near-shore component cannot be discounted, as excitation coefficients are not zero in shallower water) and short-period DF microseisms are mainly excited closer to the continental shelf slope. More recently, Koper & Burlacu (2015) showed that short and long period DF microseisms can be generated by multiple, distinct source regions during the same time period.

The use of seismic arrays provides a powerful tool to analyse propagating waves comprising a diffuse noise field. Filtering by slowness, azimuth and frequency can increase the signal amplitude allowing study of arrivals unresolvable by a single station (e.g. Burg 1964; Rost & Thomas 2002, 2009). By beamforming seismograms between stations within the array at a variety of slownesses and azimuths for a particular frequency band, it is possible to determine and distinguish the direction and velocity of multiple wave packets propagating across the array during a given time period. The use of arrays to study microseism surface and body waves have been highly successful in locating noise sources, especially when combining data sets of multiple arrays around the world (e.g. Koper *et al*. 2010; Landès *et al*. 2010; Euler *et al*. 2014).

Many microseism source studies have focused on northern hemisphere data sets (Bromirski & Duennebier 2002; Kedar *et al*. 2008; Koper *et al*. 2009; Ardhuin *et al*. 2011; Bromirski *et al*. 2013; Liu *et al*. 2016). Recently there has been a view to extend source locations more globally to include the Southern Ocean (Gerstoft *et al*. 2008; Landès *et al*. 2010; Stutzmann *et al*. 2012; Traer *et al*. 2012; Euler *et al*. 2014; Reading *et al*. 2014; Gal *et al*. 2015). However, none of these array-focused studies include similar array data from Antarctica. The location of Antarctica makes it an ideal location for understanding the factors important for noise generation in various frequency bands. Numerous strong storms migrate around Antarctica in the Southern Ocean that surrounds the continent. Sea ice builds out along the coastline during the winter months and can extend over the edge of the continental shelf, reducing microseism generation by eliminating ocean wave forcing on the continental shelf (Webb 1998; Grob *et al*. 2011; Anthony *et al*. 2015). This natural experiment afforded by changing sea ice conditions allows us to investigate the locations off the coast where microseisms are generated.

The study of microseisms in Antarctica has thus far been restricted by the distribution and configuration of seismic arrays. Dense seismic arrays in Antarctica have so far been limited to small, temporary deployments mainly used to study cryoseismicity (e.g. Blankenship *et al*. 1987; Winberry *et al*. 2013; Pratt *et al*. 2014) and volcanic sources (e.g. Rowe *et al*. 1998). More permanent arrays have recently been installed on the continent (e.g. Neumayer Watz-Array, part of the GEOFON program located in Coats Land), however these are either narrow aperture arrays, not well-suited to microseism studies, or large regional networks (e.g. TAMSEIS, GAMSEIS and POLENET/ANET) designed to study the Earth structure (e.g. Lawrence *et al*. 2006; Heeszel *et al*. 2013). These larger networks were utilized to study microseism power spectral density in Antarctica (Grob *et al*. 2011; Anthony *et al*. 2015); however, the microseism sources have not been located or studied.

In this paper we use an Antarctic seismic array deployed over the 2010–2011 austral summer to study the effect of storms and sea ice on the generation of microseisms in the Southern Ocean. Although the array was deployed for less than two months, the sea ice extent changed dramatically, falling from 12.286×10^6 km^2 on 2010 December 12, to 3.019×10^6 km^2 on 2011 January 31 (Cavalieri *et al*. 1996, updated yearly), a decrease of 75.4 per cent (Fig. 1). As well as studying the microseism noise levels throughout the two-month deployment, we also monitor daily azimuthal microseism variations for the first time for an Antarctic based

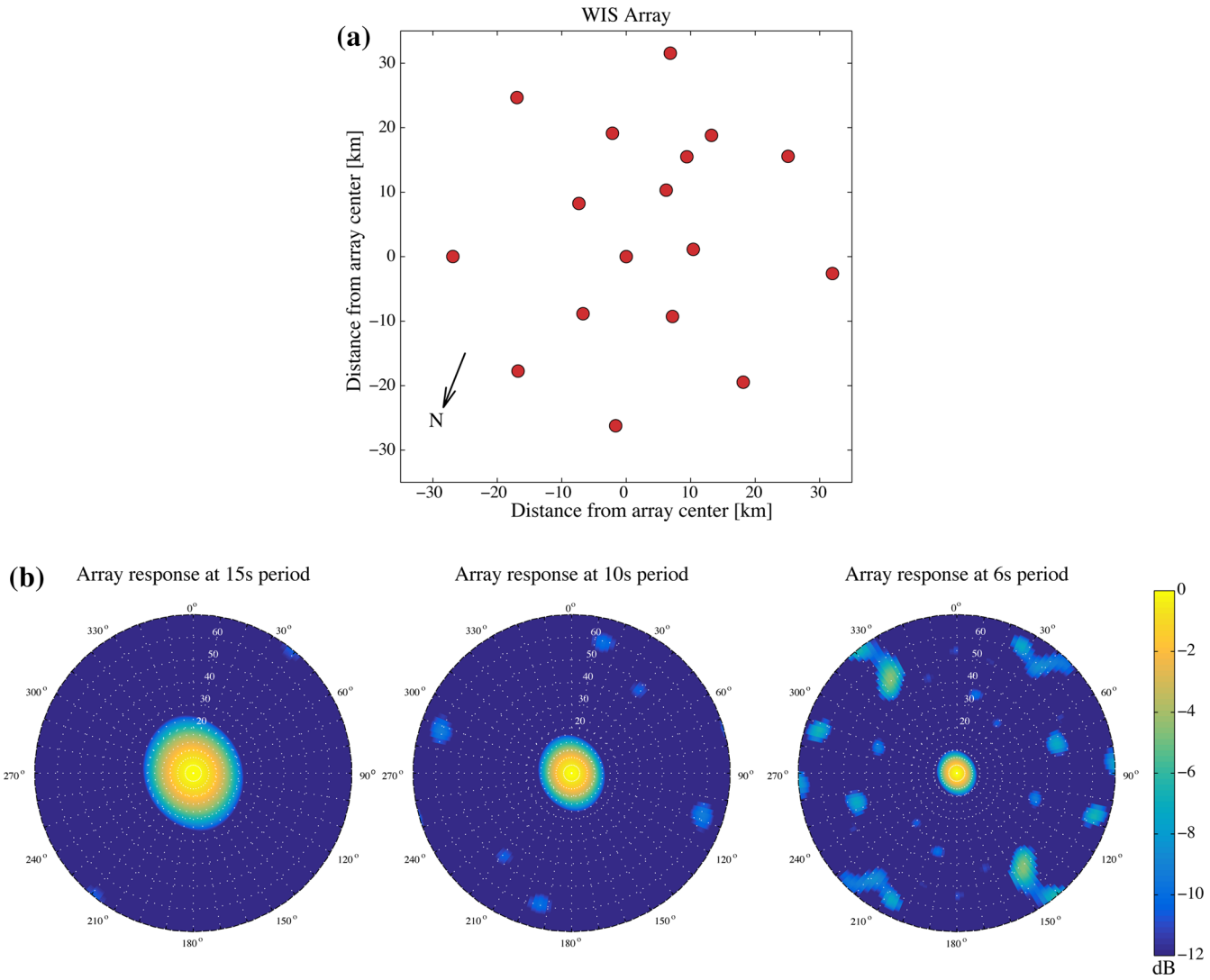

Figure 2. (a) Map of the 17 WIS Array stations used in this study. Note that the map is oriented with up corresponding to grid north (the convention used for polar maps in this study) while the azimuth for true north is marked by the arrow. (b) Array response functions for a unit amplitude incident wave with slowness of 0 s deg^{-1} (i.e. vertically incident) at periods of 15, 10 and 6 s. Response functions are truncated at −12 dB to focus on the more significant slowness aliasing features. The projection used for all *f*–*s* plots, excluding back projections to specific global locations, is oriented towards 'grid north', consistent with the map projections.

array. This data set provides important insights about the excitation mechanisms of SF and DF microseisms.

2 DATA

We analyse data from a moderate aperture (∼60 km) seismic array deployed on the Whillans Ice Stream (WIS) originally designed for glacial studies (Winberry *et al*. 2013, 2014; Pratt *et al*. 2014; Fig. 2a, Supporting Information Table S2.1), as well as two long-duration POLENET/ANET broad-band seismometers (MPAT and SURP). The power spectra of the ambient noise field collected by the WIS Array in context with MPAT and SURP are discussed in Supporting Information Section 1.

The WIS Array operated from 2010 December 12 to 2011 January 30 and consisted of 17 Nanometrics Trillium 120PA broad-band stations arranged in staggered concentric circles around an array centre of 84.2955°S, 158.1631°W (Station BB01). The offset of the stations from a regular grid pattern helps optimize the array response function by minimizing geometric artefacts known as slowness aliasing (Haubrich 1968; Kværna 1989; Kennett *et al*. 1995). Furthermore, this roughly circular arrangement provides excellent azimuthal resolution consistency that would not be as uniform for a linear or cross array (e.g. Rost & Thomas 2002).

To describe the performance of the array for resolving wave slowness in the microseism bands, we produce the array response function (ARF) for a plane wave arriving with a slowness of 0 s deg^{-1} to best show spatial artefacts (see Rost & Thomas 2002 for a full description). The resulting ARF shows that the array has good resolution and only minor artefacts across the microseism band (Fig. 2b), with the possible exception of spatial artefacts for 6 s periods at 145° and 325° that may interfere with identification of fundamental mode Rayleigh wave phase velocities at 35–40 s deg^{-1}. To aid comparison to geographic features, 0° azimuth on these polar plots is relative to 'grid north'. Grid north is a convention used in the Antarctic, where 0° is the prime meridian.

3 METHODS

3.1 Correlograms

It has long been established that a coherent signal representing the Green's function (or the response of the Earth to an impulsive source) can be extracted by the cross-correlation of the ambient seismic noise of two contemporaneous time-series (Weaver & Lobkis 2001a,b; Shapiro & Campillo 2004). Stacks of windowed cross-correlations increase the signal-to-noise of the Greens functions allowing study of emergent waves travelling between two stations. The highest amplitude signals are the surface waves that are by far the most utilized in ambient noise tomography studies (e.g. Larose *et al*. 2005; Gerstoft *et al*. 2006b).

Seismic time-series were windowed every 10 min (with a 5 min overlap), processed following steps in Benson *et al*. (2007) including a frequency-domain normalization with a 2 mHz running absolute mean, and correlated with all other stations in the array producing constraints on wave propagation along 136 unique paths. These correlograms were then stacked, per day and then by month as the signal-to-noise ratio for microseisms generally increases with the length of the time-series. This method destroys any amplitude information due to time- and frequency-domain normalization. However, this approach does allow improvement to the signal for investigation into the propagation speed and direction of microseismic surface and body wave energy. Earthquakes are not removed from the time-series but are effectively suppressed due to the processing steps and averaging. Even so, if an earthquake magnitude is large enough ($\sim M \geq 6$) it will overshadow the shorter-period microseisms over the course of that particular day. This allows us to check our back projection technique by comparing to known locations of large earthquake epicentres.

3.2 Beamforming and back projection

We beamform the daily and monthly sets of stacked correlograms for each particular microseism band over a range of horizontal slowness magnitudes and azimuths to analyse wave propagation across the array. A conventional frequency–wavenumber (*f*–*k*) approach (e.g. Rost & Thomas 2002) is used to estimate the frequency–slowness (*f*–*s*) spectrum which assumes that the wavefield is stationary over the duration of the windowed stacks. The array power, P , as a function of frequency and slowness is described by (e.g. Rost & Thomas 2002, 2009; Euler *et al*. 2014):

$$P\ (f, s) = \frac{1}{N^2} \sum_{i=1}^{N} \sum_{j=1}^{N} C_{ij}\,(f)\, e^{-i2\pi f \mathbf{s}\left(x_j - x_i\right)}, \tag{1}$$

where N is the number of stations, and C_{ij} is the cross-spectra between those stations. $\mathbf{s}$ is the slowness vector in the direction of the wave source and $x_j - x_i$ describes the distance between the station pair. The *f*–*s* spectra are then averaged over a frequency band on interest:

$$P\,(s) = \frac{1}{M} \sum_{f=f_1}^{f_2} P\,(f, s)\,, \tag{2}$$

where M is the number of discrete frequencies between f_1 and f_2.

Peaks in the *f*–*s* spectra identify the azimuth of coherent waves, but care must be taken that these are not spatial aliasing artefacts generated by the array response. The slowness of the peak helps to identify the phase, for example, Rayleigh waves will propagate at about 30–40 s deg^{-1} depending on the frequency. Body waves are much faster (<9 s deg^{-1} for teleseismic arrivals) and their origin distance can be calculated from the ray parameter by back projecting to the apparent source location at the Earth's surface. There can be some ambiguity, as for example, both *P* and *PP* phases arrive at slownesses between 4.5–9 s deg^{-1} (see Supporting Information Fig. S2.1 for explanation of the ambiguity). We use significant wave height hindcasts (Tolman 2009) to help overcome this ambiguity in determining whether arrivals are *P* or *PP* phases. We also apply back projection to core phases such as the *PKP* branches ab, bc and df (Supporting Information Fig. S2.1).

3.3 Modelling double-frequency microseisms

Recently, the theory put forth by Longuet-Higgins (1950) has been applied to DF microseisms generated in the deep ocean (Kedar *et al*. 2008; Ardhuin *et al*. 2011; Kedar 2011). Ocean gravity waves travelling in opposing directions with similar frequencies interfere and produce standing waves in the ocean column at twice the frequency. The associated surface pressure fluctuations excite seismic waves in the crust directly below that propagate away from the source region. Path effects of geometric spreading, attenuation and local structural amplification must also be considered to model the microseism amplitudes.

To model DF microseism Rayleigh waves, we use the methodology of Ardhuin *et al*. (2011, 2013) and the WAVEWATCH III model hindcasts of wave periodicity distributed by NOAA (Tolman 2009). By taking the wave spectra, applying a bathymetric excitation coefficient, and correcting for attenuation and geometric spreading, it is possible to model the noise spectrum at any location on Earth between the periods of 2 and 12 s. From Stutzmann *et al*. (2012):

$$F_p\ (\mathbf{K} \simeq 0,\ f_2 = 2f) = \rho_w^2\, g^2 f_2 \int_0^{\pi} F(f, \theta) F(f, \theta + \pi) \mathrm{d}\theta, \tag{3}$$

where, ρ_w is the density of water, g is acceleration due to gravity, f is the ocean wave frequency. $F(f, \theta)$ and $F(f, \theta + \pi)$ are the wave height spectral density for the same frequency at opposing azimuths. $F_p(\mathbf{K}, f)$ are the pressure fluctuations with wave number $\mathbf{K}$ (the sum of the wave numbers of the two opposing waves) with frequency $f_2 = 2f$. F_p has units of N^2 m^{-2} Hz^{-1}. For this analysis we use the 0.5° resolution hindcasts downloaded from the IOWAGA archive (http://www.ifremer.fr/iowaga/Products) which are derived from the WAVEWATCH III model. We utilize maps of the noise source (in metres) at each period band from these hindcasts to interpret the provenance of microseisms. One consideration that has been implemented in these hindcasts that is useful in the interpretation of our data is the effect of coastal reflection causing wave–wave interactions. The method of Ardhuin *et al*. (2011) allows for a range of reflection effects, between no coastal reflections and reflections of which 10 per cent are from mainland coastlines, 20 per cent from small islands and 40 per cent from icebergs.

The seismic source power spectral density S_{DF} in m Hz^{-1}, at the ocean bottom is therefore (Longuet-Higgins 1950; equation 186):

$$S_{DF}\ (f_s = f_2) = \frac{2\pi f_s}{\rho_s^2 \beta^5} \left[\sum_{m=1}^{N} c_m^2 \right] F_p\,(\mathbf{K} \simeq 0,\ f_2 = 2f)\,, \tag{4}$$

where ρ_s and β are the density and shear velocity of the crust respectively. $f_s = f_2$. c_m coefficients correspond to the compressible ocean amplification factor, depending on the ratio $2\pi f_2 h/\beta$, where h is the water depth (see Supporting Information Fig. S2.2). F_p describes the ocean wave pressure fluctuations in N^2 m^{-2} Hz^{-1}.

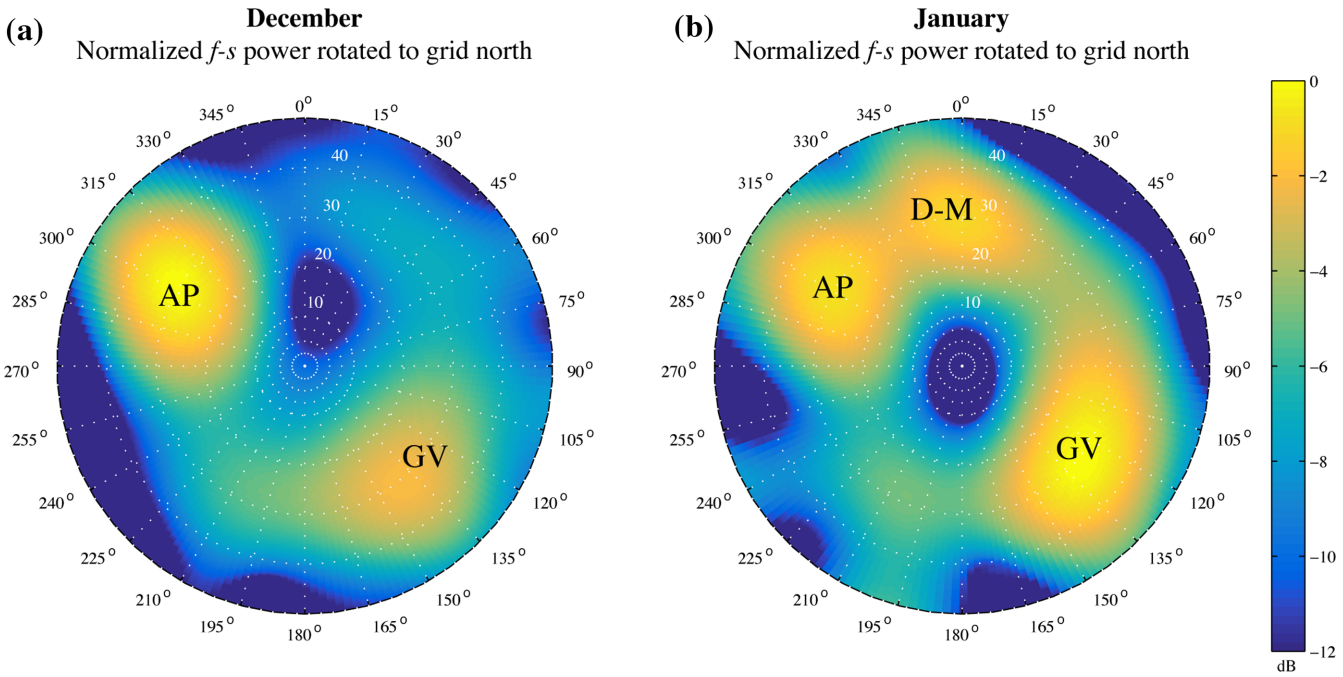

Figure 3. Monthly SF microseism *f–s* maps averaged over periods 13–16 s and rotated to grid north. Amplitude is in decibels normalized to the maximum amplitude. (a) December 2010 showing the strong peaks at fundamental mode Rayleigh wave phase velocities in the direction of the Antarctic Peninsula (AP) and a broad, relatively lower peak in the direction of George V Land (GV). (b) January 2011 showing the additional peak in the direction of Dronning–Maude Land (D–M). Geographic projection of the Rayleigh wave energy is shown on Supporting Information Fig. S2.6(a).

Adding the path effects for both attenuation and geometric spreading, we can discretize the ocean forcing and define the spectral density F_δ, in $m^2\ Hz^{-1}$ at any particular colatitude, ϕ, and longitude, λ, by integrating the sources along the path length (Stutzmann *et al.* 2012):

$$F_\delta\ (\lambda, \phi, f_s) = \int_0^{2\pi} \int_0^{\pi} \frac{S_{\mathrm{DF}}\,(f_s)}{a \sin(\alpha)} P\,(f_s) \times \exp\left(\frac{-2\pi\, f_s a \alpha}{Q\,(f_s)\, U\,(f_s)}\right) a^2 \sin\left(\phi'\right) \mathrm{d}\lambda' \mathrm{d}\phi', \qquad (5)$$

where a is the radius of the Earth, α is the angular epicentral distance and $a^2 \sin(\phi')\mathrm{d}\lambda'\mathrm{d}\phi'$ is the elementary surface area. $P(f_s)$ is a dimensionless parameter to account for 3-D propagation, or local, amplification effects, this variable is ignored as there are limited constraints on its value. $Q(f_s)$ and $U(f_s)$ are the attenuation and Rayleigh wave group velocity respectively (Stutzmann *et al.* 2012). Using this theory, we are able to compare the modelled DF microseismic noise generated by Southern Ocean storm systems with noise observations at the WIS Array.

The methods used in this paper do not directly allow comparison of amplitudes in the model to amplitudes measured from the WIS array. However, it is shown in Supporting Information Fig. S2.3 that modelled amplitudes for January match those for station BB01 when certain criteria are met. It is clear that reflections are important to provide enough energy to generate the observed spectra for reasonable values of Q. It is likely that the reflection coefficients are highly variable in the Southern Ocean due to increases in iceberg production during the summer months, so to simplify we choose the maximum values for the reflection coefficients. With this we found that setting Q to 400 and 300 for the long-period and short-period DF bands respectively provided satisfactory fit to the observed spectra.

4 THE SEISMIC NOISE FIELD OF THE ANTARCTIC INTERIOR

4.1 Single-frequency microseism band

We focus on SF microseisms by filtering monthly stacks of correlograms at 13–16 s. The *f–s* plots have been rotated to grid north and are shown in Fig. 3. The December 2011 map shows two distinct backazimuths at surface wave slownesses. The strongest signal is from 305°, the direction of the ice-free Antarctic Peninsula, and a weaker signal comes from 135°, the direction of George V Land where sea ice extent is relatively small (Fig. 1). The January 2011 slowness map exhibits a third backazimuth showing a strong surface wave signal at 0°, the direction of Dronning-Maude Land. This part of Antarctica becomes relatively ice-free during the summer months, opening up the continental shelf to storm swells (Fig. 1). Furthermore, the relative amplitude of the signals shows that the 135° source becomes stronger in comparison to the 310° Peninsula source reflecting that the continental shelf in the George V Land region becomes significantly free of sea ice.

Fig. 4 provides a summary of daily SF data comparing the grid north oriented slowness maps and the WAVEWATCH III significant wave height model. This provides indication to where coastal swell should be highest along the coast lines. During the time of the deployment the daily *f–s* maps show the three sources vary roughly in correlation to the locations of Southern Ocean storms. The highest amplitude source fluctuates initially through two backazimuth directions of ∼310° and 135°, and later in the season through three directions including the 0° source. The 310° source from the direction of the Antarctic Peninsula is the most frequent maximum.

The relative amplitude of the SF microseism peaks observed by the WIS Array show that the source in the direction of 135° becomes stronger from December to January in comparison to the Peninsula source indicating that the continental shelf in the George V Land

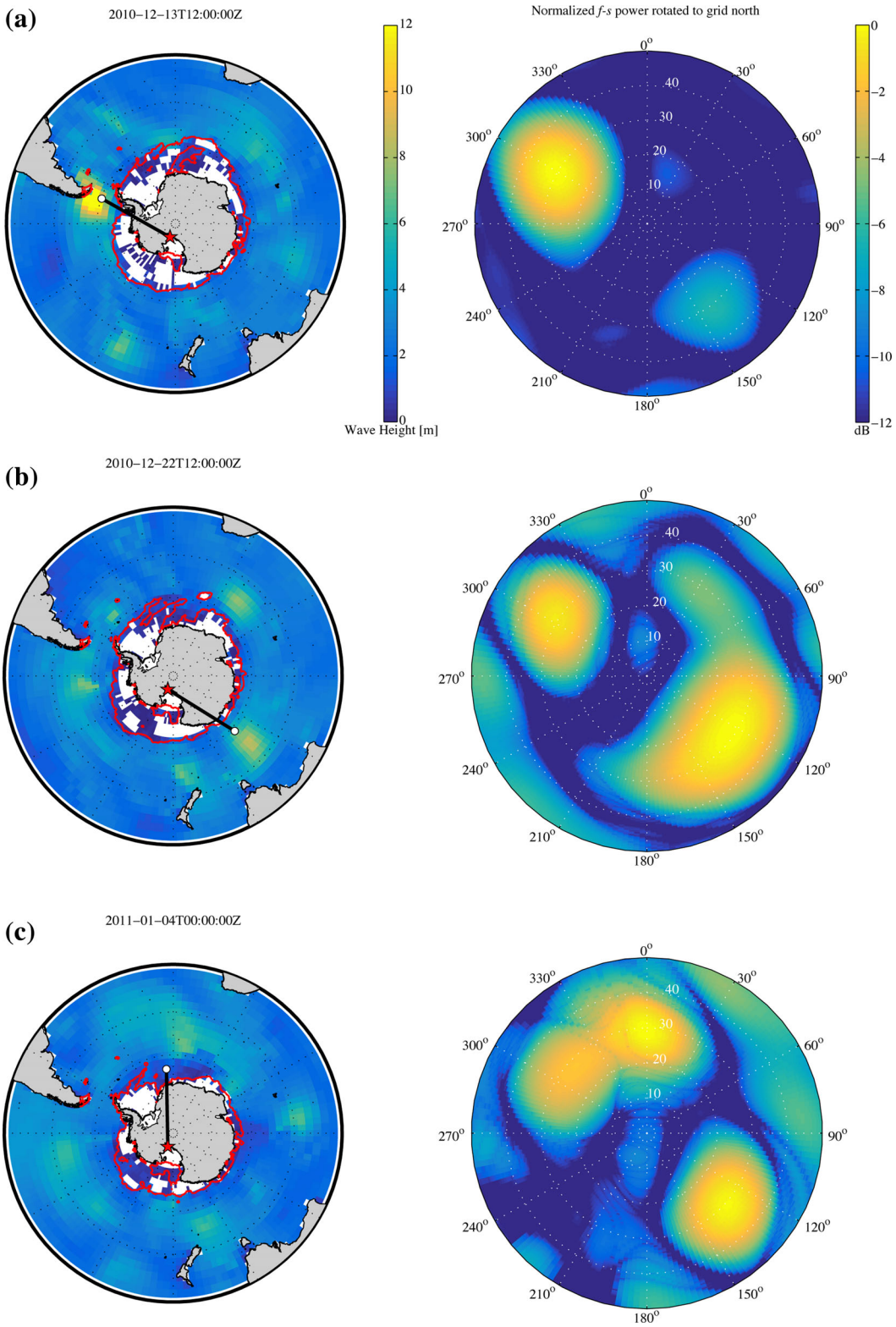

Figure 4. Comparison of significant wave height from WAVEWATCH III (left column) and daily SF microseism *f–s* maps in the SF microseism band (right column). Red line marks sea ice extent for that day, red star marks the location of the WIS Array. The black line with white circle marks the azimuth of the strongest observed Rayleigh wave peak, the length of the line is arbitrary as no distance information is available.

region becomes significantly free of sea ice. Each peak is excited generally when high amplitude ocean waves are in one of the three regions. The variation in the *f–s* plots of the monthly SF microseism sources show the addition of the Dronning-Maude Land source after the 4th of January 2011 (Fig. 4; Supporting Information Fig. S2.7). Interestingly the Dronning-Maude Land becomes much stronger in amplitude compared to the relatively sea ice-free regions of the Antarctic Peninsula and George V Land. This observation correlates

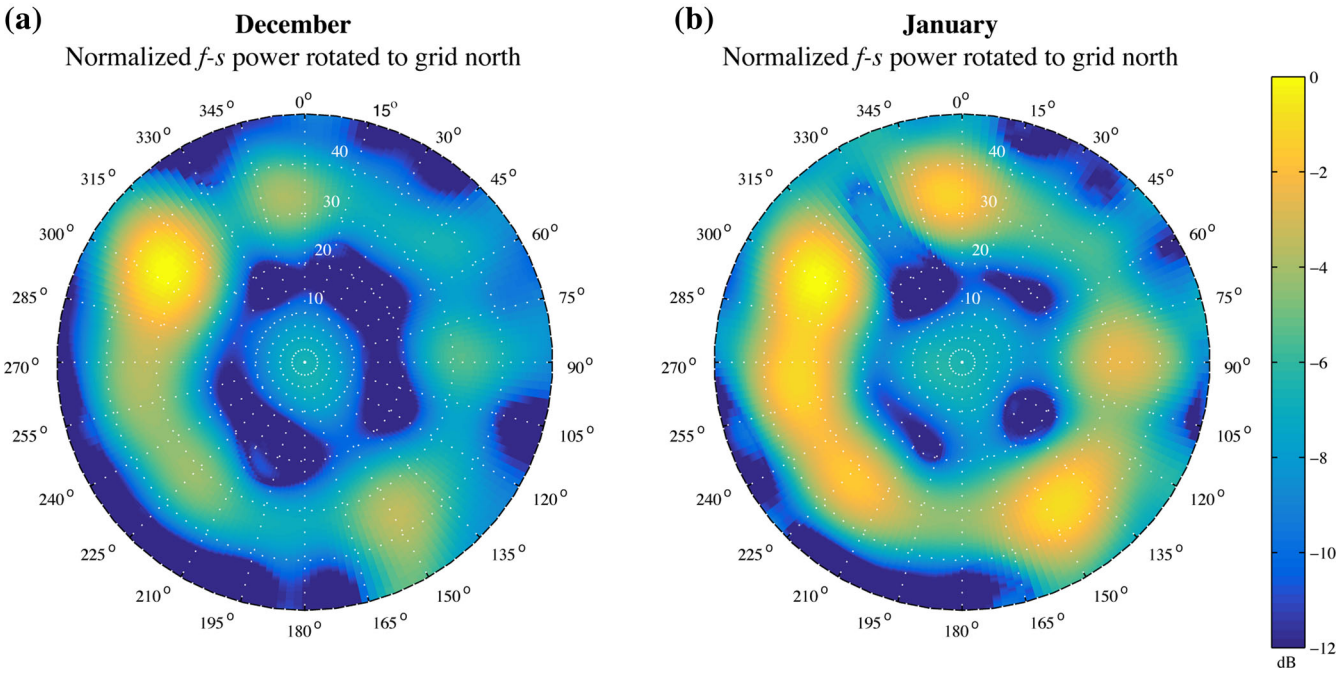

Figure 5. As Fig. 3 but for LPDF microseism band of 9–11 s periods. Geographic projection of the Rayleigh wave energy is shown on Supporting Information Fig. S2.6(b).

with significant sea ice loss during the summer months allowing waves to shoal over the continental shelf in this region. This has been shown to be an SF microseism source region that becomes active over the late austral summer months from POLENET/ANET and GAMSEIS data (Koch *et al*. 2013).

Potential long-term deployments in Antarctica should expect to observe changes in SF source location as sea ice concentrations change with the changing climate. Although sea ice extents have remained fairly stable over the last 30 yr compared to the Arctic Ocean (e.g. Simmonds 2015), analyses of SF noise locations provide ground-based observations that may highlight specific regions of increasing or diminishing sea ice.

4.2 Long-period double-frequency microseism band

The LPDF microseism band (Fig. 5) shows strong Rayleigh wave signals arriving in December from 315° (Antarctic Peninsula) and smaller amplitude source directions at 150° (George V Land) and 355° (Dronning-Maude Land) that are similar to the SF microseism band. Energy is also seen to be arriving between 210° and 285°, which is the direction of the Marie Byrd Land Coast, which has extensive sea ice. The January slowness map has a similar arrangement of sources to December. The relative intensities of non-Peninsula sources are amplified in January, suggesting a more prevalent source (e.g. more storms), a change of coupling conditions (e.g. a reduction in sea ice), or both. Large peaks are similar to those in the SF microseism band suggesting there may be some leaking of the SF microseism signal into this band. A factor that may explain the relative amplitude increase in January is the effect of coastal and iceberg reflections generating interfering waves, as well as storms encroaching closer to the continental shelf thus reducing propagation effects. Icebergs generally exhibit near vertical sides producing a high reflection coefficient (Ardhuin *et al*. 2012). Additionally, considering the high amplitude of LPDF microseisms throughout the year and given that sea ice extent dampens many coastal swell reflections, we interpret the year-long LPDF energy as originating in the deep ocean.

A notable feature of this band is the absence of signal at 330°, and a diminishment in signal power at 185°. These backazimuths are in the direction of the Ronne-Filchner and Ross Ice Shelves respectively. Relatively large concentrations of sea ice remain prevalent throughout December and January in these directions. It is possible that the increased source distance, coupled with limited fetch lengths as the sea ice breaks up, restricts the potential of microseisms to be generated within this LPDF band.

We model LPDF microseism source locations using the eqs 3–5 (Ardhuin *et al*. 2011; Stutzmann *et al*. 2012) using hindcasts generated by IFREMER model parameterization (ftp.ifremer.fr). This allows us to calculate the displacement contribution of the source at locations in the Southern Ocean using bathymetry from WAVEWATCH III global 0.5° resolution data set. We then compare beamformed daily stacks of the noise correlograms at 9–11 s to daily averages of wave–wave interaction calculations (Fig. 6). Propagation is modeled using an apparent Q of 400 and a Rayleigh wave group velocity of 3.8 km s^{-1}.

The most striking feature of this frequency band is the ability to track storms each day in the Southern Ocean, particularly the South Pacific. Here sources are located in the deep ocean away from Antarctic coastlines, although the model input includes effects from coastlines and sea ice. Fig. 6 also shows that the noise source provides information on the relative strength of different storm systems. The relatively low peak on December 29th develops into a much stronger signal by December 31st as the noise source in the Amundsen Sea broadens and strengthens compared to those south of Australia.

4.3 Short-period double-frequency microseism band

The SPDF microseisms, shown for the 5–6 s band (Fig. 7), display a less obvious pattern of peaks. Comparison with the ARF (Fig. 2b)

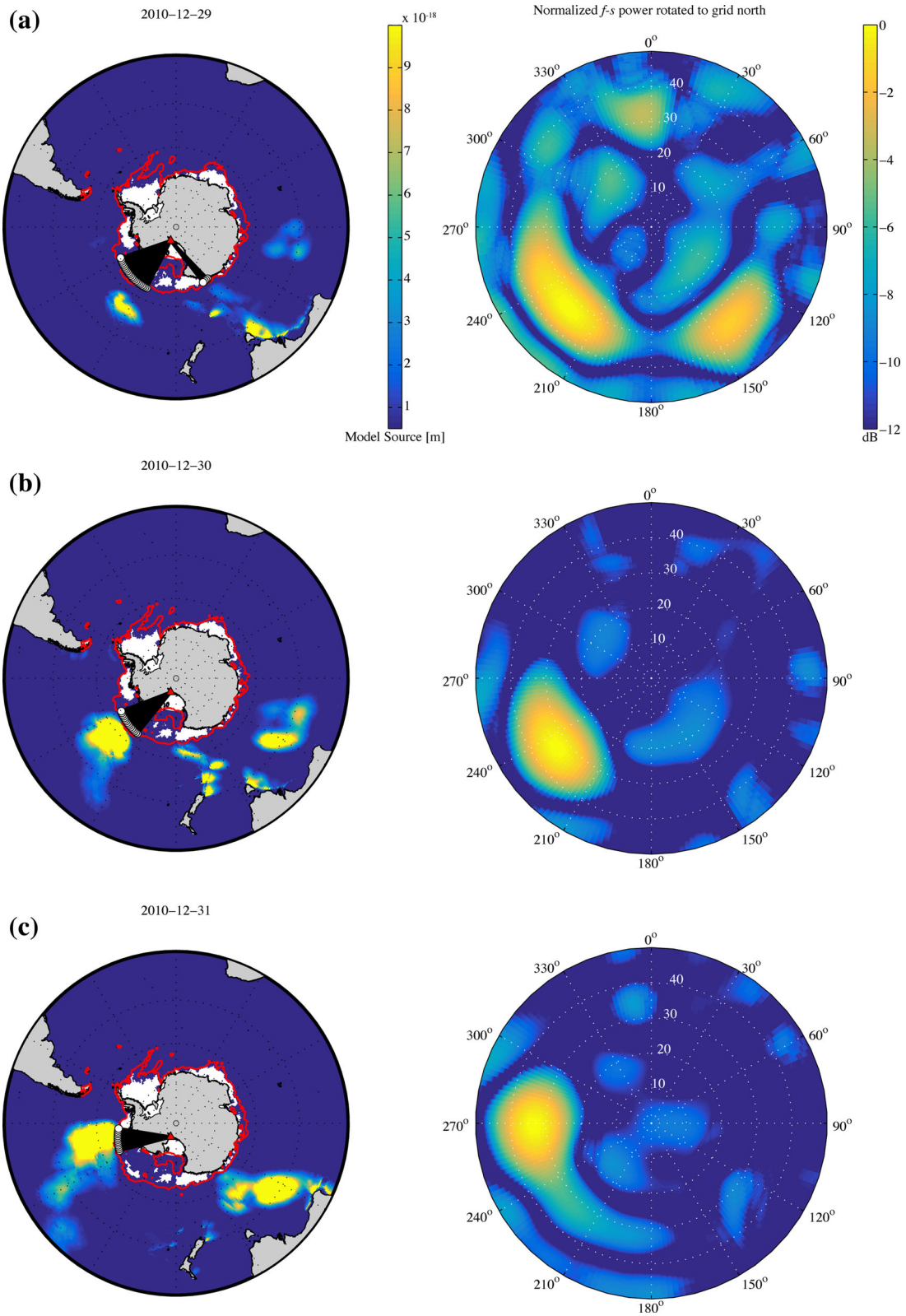

Figure 6. Comparison of daily averaged source locations from the DF microseism model of Ardhuin *et al.* (2011) at 10 s period (left column), and the daily *f–s* maps at 10 s (right column). The modelled source maps show the contributions of each ocean location to the DF microseism at this band (eq. 5, pre-integration) Three consecutive days are shown, black lines with white circles show azimuths with observed microseism energy >-2 dB. Rayleigh wave energy recorded at the WIS Array appears to closely track a strengthening DF microseism source caused by a storm system in the Southern Ocean.

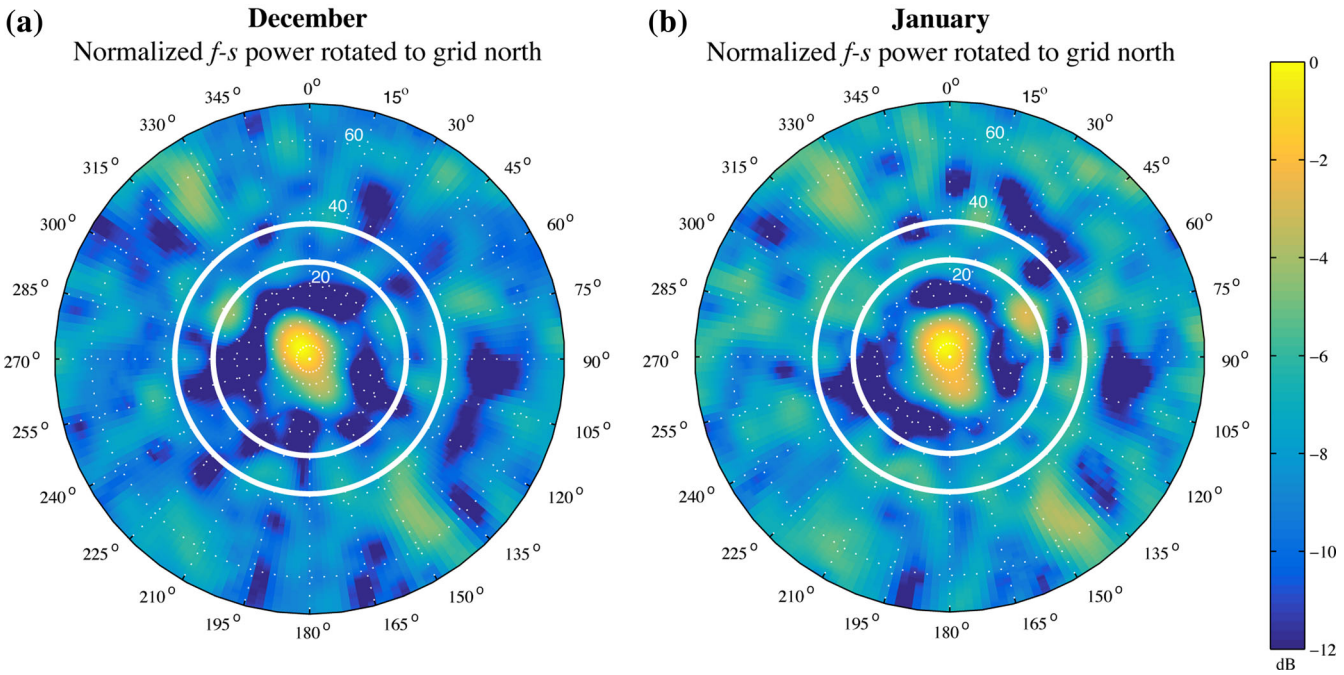

Figure 7. Monthly *f–s* maps for the 5–7 s period band. Two white circles are at slownesses of 37 s deg^{-1} and 26.5 s deg^{-1} corresponding to fundamental Rayleigh waves and *Lg* respectively. Note that we extended the slowness axis (radial) compared to previous figures to illustrate the peaks at 50 s deg^{-1} and 145° and 325° azimuth that are array geometry artefacts from the strong peak centred around 0 s deg^{-1}, which is likely the result of poorly resolved body waves. Geographic projection of the *Lg* energy is shown on Supporting Information Fig. S2.6(c).

suggests the presence of array artefacts for both months at backazimuths of 145° and 325° with 50 s deg^{-1} slowness. The white circle at 37 s deg^{-1}, highlighting the region where the fundamental mode Rayleigh wave is expected to arrive, shows no prominent peaks for either month. However, the slowness circle of ∼26.5 s deg^{-1}, corresponding to a velocity of 4.19 km s^{-1}, shows much clearer peaks in December at 300° (Antarctic Peninsula) and particularly in January at ∼60° towards the Amery Ice Shelf region. The large peak near slowness of zero is most likely due to body wave energy that is stronger in the SPDF band than in the LPDF band. As these maps are calculated using month-long stacks, the near zero slowness peak represents an average of many body wave sources and so is broadened such that we cannot make an accurate interpretation of the source.

SPDF microseisms can be examined in more detail using daily stacks of 4–6 s *f–s* plots (Figs 8a–c). Strong peaks are again observed at ∼25–27 s deg^{-1} (4.12–4.45 km s^{-1}) throughout the deployment. They are unlikely to be body waves (a back projection of a *P* or *S* phase places many of the source locations in the middle of East Antarctica), are much faster than expected for fundamental mode Rayleigh waves at this frequency and, as we are only using vertical-component seismograms, cannot be Love waves. We therefore interpret these peaks as *Lg* phase arrivals because the observed slowness corresponds to typical *Lg* slownesses for continental structures (Koper *et al*. 2010; Gal *et al*. 2015). Fig. 8 also compares the *f–s* maps to modelled seismic sources (Ardhuin *et al*. 2011; Stutzmann *et al*. 2012) as in the previous section this time with an apparent *Q* of 300. Although we do not observe fundamental Rayleigh wave arrivals at this band, it is important to note where DF microseism sources may be generated.

Examining the entire suite of daily stacks, we find *Lg* arrivals track areas of increased DF microseism generation when they are close to the continental shelf that is relatively ice-free. Peaks with *Lg* slowness show the largest amplitude on 29 of the 50 days during the WIS Array deployment. Backazimuths of *Lg* arrivals are summarised in Fig. 9, showing the locations as if the *Lg* waves were generated at the edge of the continental shelf.

Microseism *Lg* phases are likely generated at the coastline or on the continental shelf, and propagate through continental crust (e.g. Kennett 1986). The *Lg* phase is highly sensitive to crustal thickness, suggesting that the majority of backazimuth paths should be through stable cratons. From the January slowness map, it shows that the dominant directions of the *Lg* arrivals have backazimuths that are across East Antarctica (clockwise 345°–150°) and towards the Antarctic Peninsula (300°), propagating through areas interpreted as thick, continental crust over distances of 1800–3300 km. Conversely, there is an absence of *Lg* slowness power arriving from the direction of the West Antarctic Rift System (WARS) and the Ross Sea (clockwise 195°–275°). *Lg* power at these azimuths may be related to crustal thickness variations across the WARS (Chaput *et al*. 2014; An *et al*. 2015) that would provide a significant barrier to *Lg* energy. We note though, that these arrivals originate from areas of Antarctica that are the furthest north and so experience the breakup of ice overlying the continental shelf earlier in the austral summer. The duration of the WIS Array may not have been long enough to observe storm systems interacting with the continental shelf in the Ross and Amundsen Seas.

Also within this band are body-wave arrivals observed at slownesses <10 s deg^{-1} that contribute to the overall power of this band and occasionally dominate the energy received at the WIS Array. Although the excitation coefficients used in eq. 4 are different for Rayleigh waves and *P* waves, the depth sensitivity is roughly the same (see Supporting Information Fig. S2.9). Because of the aperture of the WIS array we are unable to distinguish with confidence between different body wave phases in this band. These body wave arrivals are occasionally the highest energy signals recorded

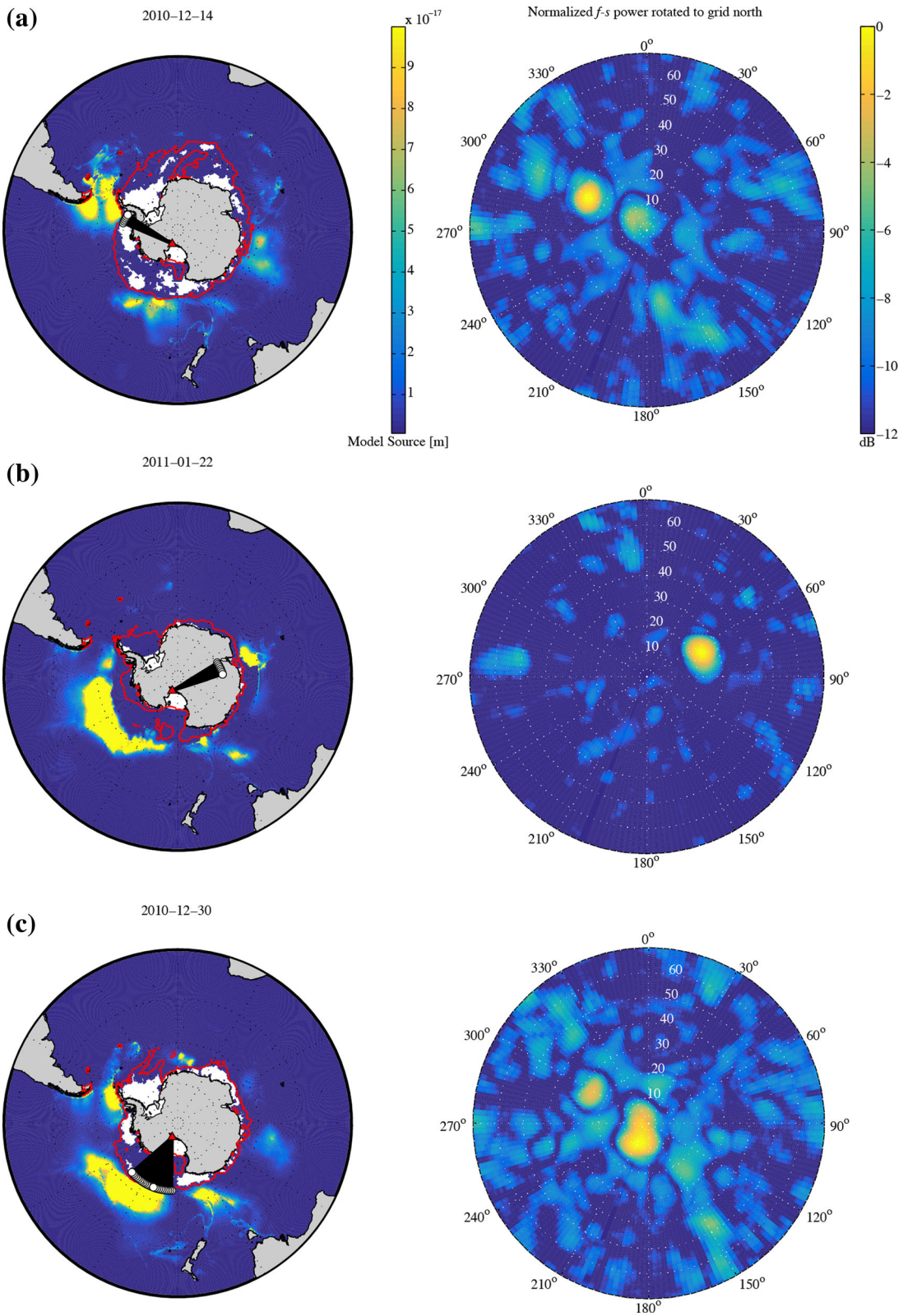

Figure 8. As Fig. 6, but for periods 4–6 s. The left column is seismic energy modelled at 6 s period based on Ardhuin *et al*. (2011). Three dates are chosen to highlight *Lg* arrivals from the direction of (a) the Antarctic Peninsula, and (b) the Amery Ice Shelf where the *Lg* arrival appears to dominate over all other sources of seismic energy at this band. (c) Highlights how the 4–6 s band records body wave energy (at low slownesses) from a large storm in the Southern Ocean that is more intense than *Lg* microseisms from the Antarctic Peninsula. For the pressure map that includes the *P*-wave excitation, see Supporting Information Fig. S2.8.

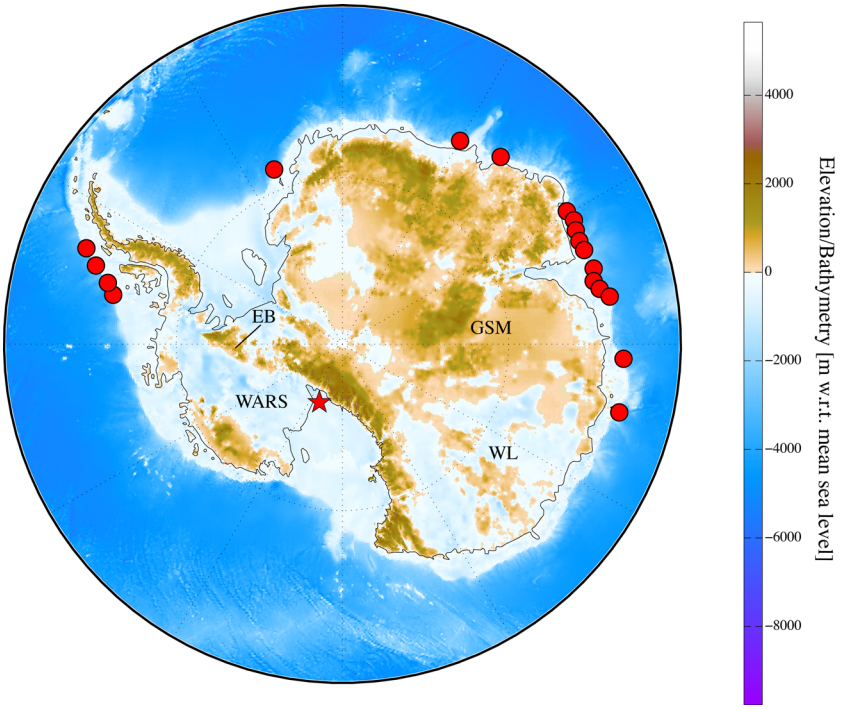

Figure 9. Direction of *Lg* arrivals back projected to the edge of the continental shelf (red circles) for each day during the WIS Array deployment when the *Lg* phase is the prominent arrival. Multiple days of the same backazimuths are plotted on top of each other. The basemap is the ice free elevation (m) of Antarctica (ETOPO1). Red star marks the location of the WIS Array. Notable geologic features: EB: Ellsworth Block (continental crust); WARS: West Antarctic Rift System; GSM: Gamburtsev Subglacial Mountains; WL: Wilkes Land.

across the WIS Array (Fig. 8c). These are likely generated by large Southern Ocean storms and are observed at backazimuths towards the Amundsen Sea, the Scotia Arc and South Africa. The source regions for these body waves can be attributed to modelled deep ocean locations (Fig. 8c). The source distance of these body waves is in excess of the influence of sea ice and is a contributor to the year-round energy observed in the SPDF band at Antarctic stations.

4.4 Ultra-short-period double-frequency body waves

At 0.3–2 s period we observe waves propagating across the WIS Array with slownesses characteristic of body waves. These arrive within the *P*/*PP* and *PKP*bc slowness ranges (Supporting Information Fig. S2.1) and are back projected accordingly. Monthly *f–s* maps (Fig. 10) show little in the way of variation between each month suggesting that sea ice has little or no effect and it is likely that bathymetry is the control on source location (Euler *et al*. 2014).

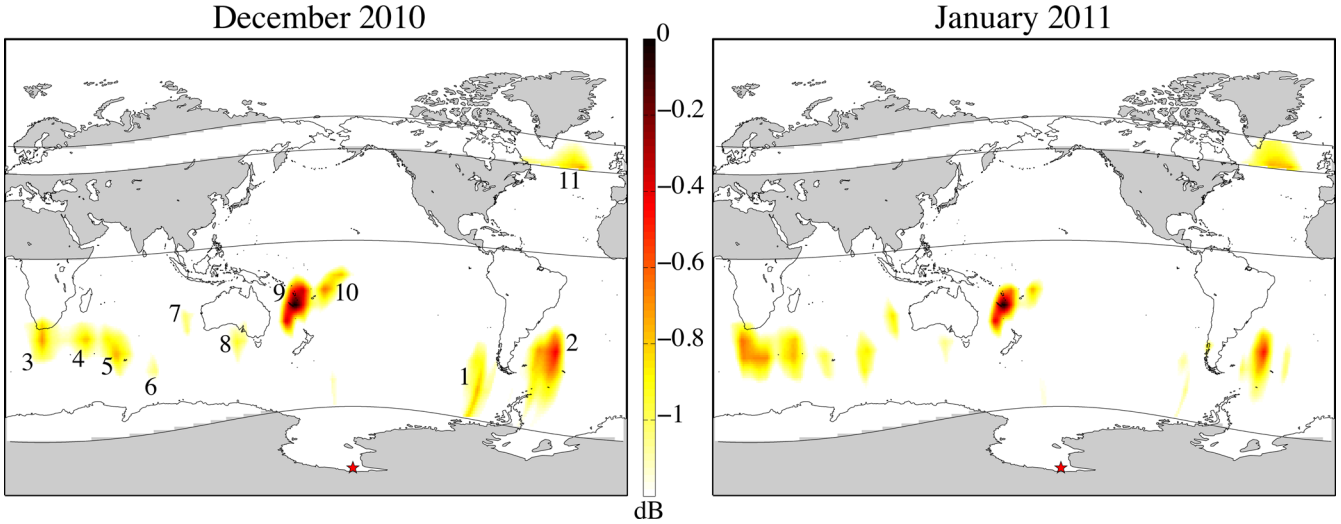

Figure 10. Monthly back projected *f–s* maps at 0.3–2 s period, showing body wave arrivals at *P*+*PP* and *PKPbc* slownesses. Bathymetric source regions are 1: Peter I Island–South Chile; 2: Scotia; 3: Cape of Good Hope; 4: Conrad Rise; 5: North Kerguelen Plateau; 6: South Kerguelen Plateau; 7: West Australia; 8: Great Australian Bight; 9: Vanuatu earthquakes; 10: Tonga earthquakes; 11: Southern Greenland. The *f–s* maps for each month are shown in Supporting Information Fig. S2.10.

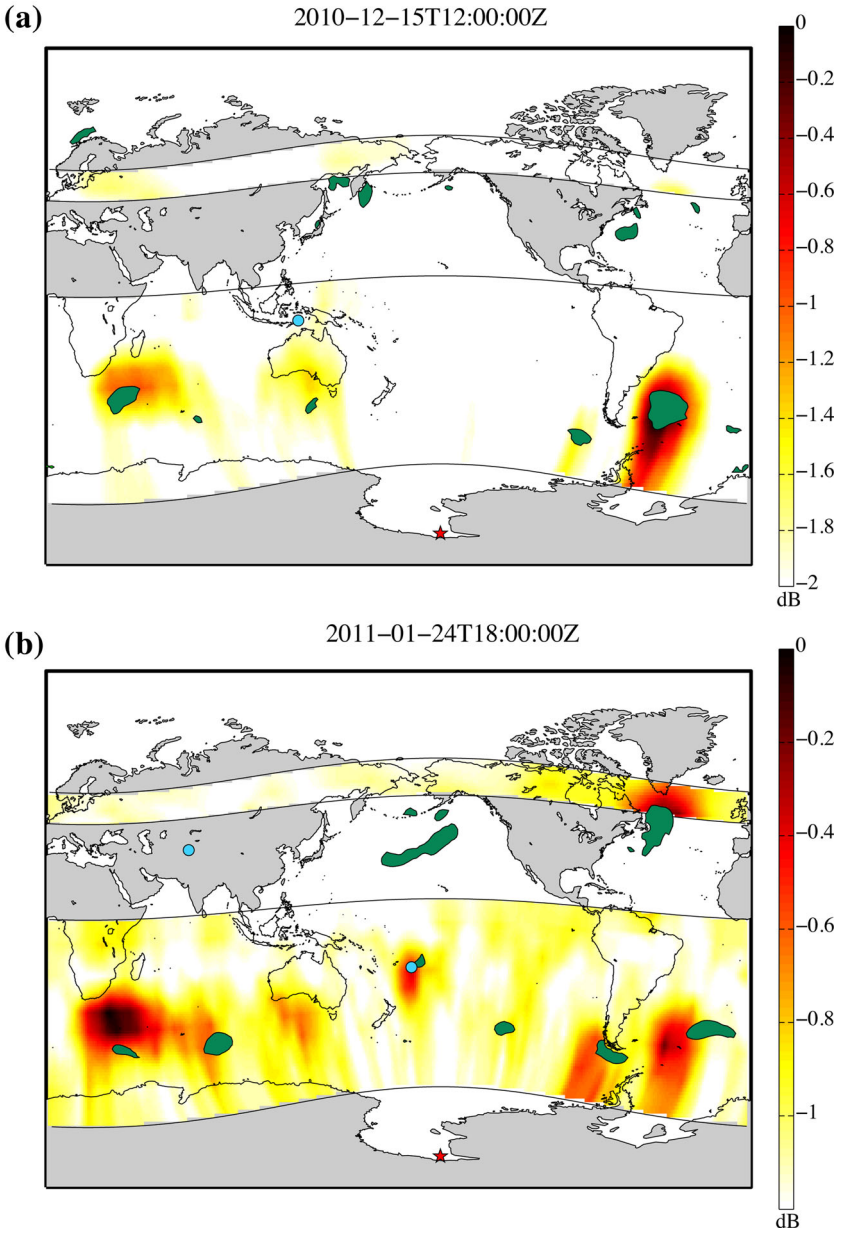

Figure 11. (a) *P* and *PKPbc* back projection of daily correlogram stack 2010-12-15, (b) back projection of daily correlogram stack 2011-01-24. Red star is the location of the WIS array. Green polygons mark areas of wave height >6 m based on the WAVEWATCH III model (Tolman 2009). Blue circles mark significant earthquake epicentres on each day: (a) Banda Sea, M_w 6; (b) Tonga, M_w 5.7; Tajikistan, M_w 6.1.

Locations of USPDF body wave sources within the Southern Ocean correlate well with previous observations (Gerstoft *et al*. 2008; Landès *et al*. 2010; Stutzmann *et al*. 2012; Euler *et al*. 2014; Reading *et al*. 2014; Davy *et al*. 2015). Locations of microseism sources appear to be related to shallower bathymetry that include ocean island chains, mid-ocean ridges and oceanic plateaus (Fig. 10).

Although there is some inherent ambiguity between *P* and *PP* phases, the correlation between the back projection and significant wave height locations suggests that these propagating phases are *P* arrivals. Fig. 11 shows back projections from two days during the WIS Array deployment overlain with regions of significant wave height (>6 m) and also significant earthquake epicentres (>M_w 5.5) during each 24 h interval.

Reflections from coastlines appear to be an important factor in providing the required environment for USPDF microseisms to be generated. Back projected locations are biased towards the coast side of maximum wave height locations (Fig. 11). Particularly strong source regions include the Scotia arc and south-east of South Africa between the Cape of Good Hope and the Kerguelen Plateau. Smaller, but not insignificant, sources are located off the coast of Australia, the most common being within the Great Australian Bight. Source regions for body wave microseisms appear to remain spatially fixed, suggesting a bathymetric control; there is little variation between the two monthly *f–s* maps (Fig. 10). The *PKP*bc source occurs at the southern tip of Greenland (Fig. 10), a region that has been well documented for microseism generation (e.g. Kedar *et al*. 2008; Ardhuin *et al*. 2011).

5 DISCUSSION AND CONCLUSIONS

We have shown the potential for studying microseism generation using an Antarctic-based moderate aperture array such as the WIS Array. Sea ice damping is not evenly applied to all types of microseisms, allowing discrimination between different possible source regions. For the SF microseism and the SPDF microseism bands, noise levels are reduced in the austral winter. Monthly *f–s* maps show that there are systematic temporal variations in noise source locations at each of the frequency bands described. It has been well documented that sea ice concentration strongly affects SF microseism generation (Grob *et al*. 2011; Tsai & McNamara 2011; Stutzmann *et al*. 2012; Koch *et al*. 2013; Anthony *et al*. 2015), and perhaps also SPDF microseism generation (Grob *et al*. 2011). The LPDF microseism shows a slight diminishment during the winter months but is never absent from the noise records. This evidence indicates that SF and SPDF microseisms are largely generated on the continental shelf and highly dependent on sea ice concentrations over the continental shelf, whereas LPDF energy is generated by storms in the deep ocean, consistent with the theory of wave-wave interaction. LPDF sources are well fit by wave-wave interaction models incorporating ocean bathymetry, and track storms circling Antarctica in the Southern Ocean.

Smaller amplitude SPDF microseisms persist throughout the winter months and likely consist of body waves from distant storms. The SPDF band increases in amplitude during the austral summer as sea ice retreats and storms interact with the coast and icebergs. Much of the summer SPDF noise generation consists of *Lg* phases generated along the exposed coastlines. We are able to tie backazimuths from beamformed SPDF microseisms interpreted as *Lg* phases to modelled oceanic sources, and the model provides a better fit to the observations when we include reflection information from coastlines and icebergs. Body waves are observed at 0.33–2 s periods and can be back projected to areas of known strong storms in both the Southern Ocean and North Atlantic.

Recent modelling by Gualtieri *et al*. (2015) provides interesting results regarding the transmission of ocean sourced seismic energy with relationship to land stations and the position of the source with respect to the coastline and sedimentary basins. The presence of a sedimentary basin at the source location provides a significant damping effect on the seismic energy, whereas sources seaward or landward of the basin still produce detectable energy. Large sedimentary basins occur around Antarctica, most significantly the Ross and Ronne Embayments. These basins extend to the edge of the continental shelf and have been observed in ambient noise studies as slow anomalies at short periods (Pyle *et al*. 2010). The enhanced attenuation from large sedimentary basins may provide an explanation for the lack of signal within the DF microseism band in these backazimuths from the WIS array. However, from our observations, LPDF energy is generated in the deep ocean beyond the extent of the sediments. It is therefore probable that lingering sea ice within the Ross and Weddell Seas, increases the distance to the source, as well as providing significant damping on LPDF microseism generation. A longer duration array would determine whether this is the case.

It has been highlighted in previous literature that icebergs and subresolution islands provide additional reflections aiding DF microseism generation. The models of Ardhuin *et al*. (2011) take into account these smaller reflections and an interpolation can be made between a 40 per cent iceberg, 20 per cent small island, 10 per cent coastal reflection coefficient model and a 0 per cent reflection coefficient model to find an adequate representation of the noise field. The reflections off icebergs is particularly important in the Southern Ocean and it has been shown that an accurate representation of the

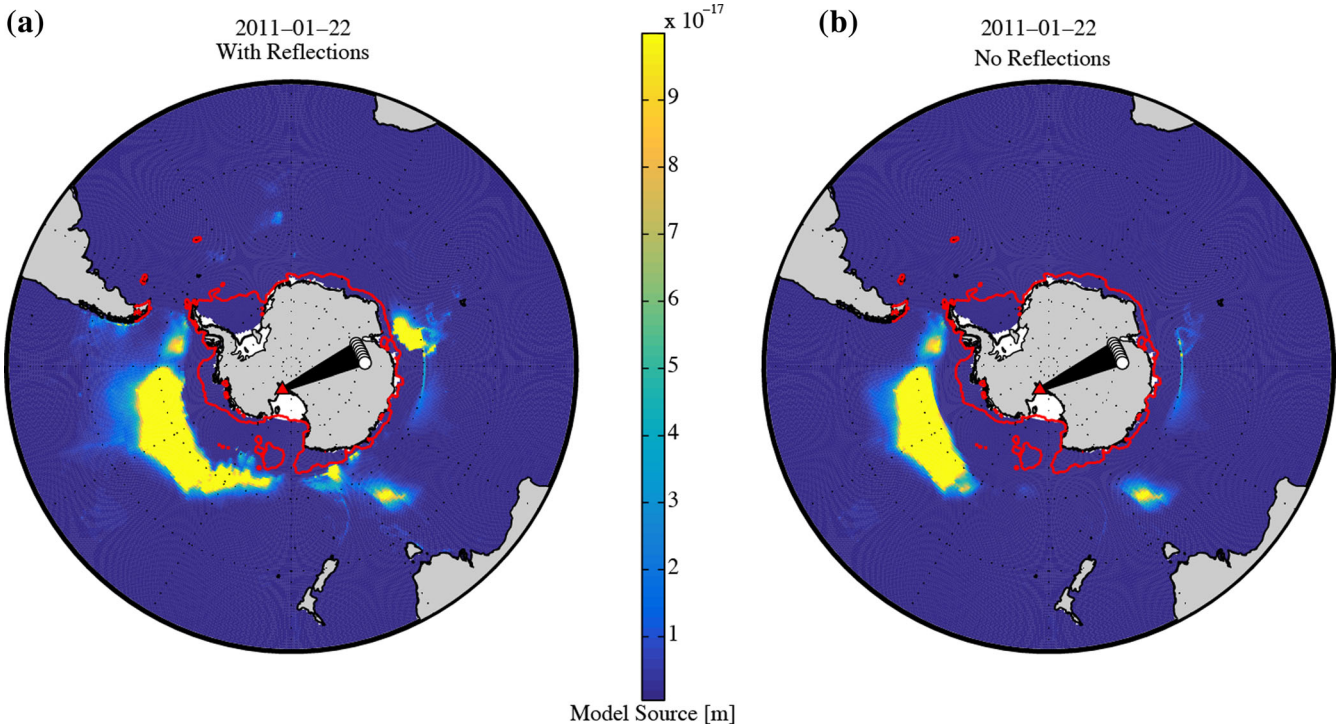

Figure 12. Model comparison showing the inclusion of (a) coastal reflections and (b) no reflections on 2011 January 22. The associated *f–s* map is shown in Fig. 8(b) displaying a strong *Lg* phase.

ocean wave field cannot be made without taking these reflections into account (Tournadre *et al*. 2008; Fig. 12). We find that including reflections within the model are important in the Southern Ocean. Our results particularly indicate this at shorter periods, where excitation maxima of the DF microseism is closer to the Antarctic continent, and there is the potential for a higher abundance of reflections from icebergs.

We have shown in this paper that seismic array analysis allows the tracking of storm systems and sea ice concentrations from ground based data. This is particularly apparent in polar regions, enhancing climatic and oceanographic information with seismic noise information can be implemented as a proxy for sea states. Path information may be inverted from travel-times and amplitudes provided enough information is known about the source region and mechanism for generating microseisms. At the frequencies of microseism energy this will illuminate crustal structure, potentially allowing the exploration of regions that are not easily accessible with large seismic networks.

ACKNOWLEDGEMENTS

Our thanks also go to the Incorporated Research Institutions for Seismology/Portable Array Seismic Studies of the Continental Lithosphere Polar Group for supplying equipment and support. This work was supported by the U.S. National Science Foundation Office of Polar Programs grants ANT-0944671 and ANT-0632209. Thanks also go to Audrey Huerta, Rick Aster, Terry Wilson and Andy Nyblade for supplying additional The Polar Earth Observing Network seismic data, and the other members of the WIS Array deployment team: Alex Brisbourne, Peter Burkett, Randy Justin, and Stephanie Kay. Finally, we thank Raytheon Polar Services, Ken Borek Air, and The New York Air National Guard for providing logistics in Antarctica.

REFERENCES

Amante, C. & Eakins, B.W., 2009. ETOPO1 1 Arc-minute global relief model: procedures, data sources and analysis, NOAA, Technical Memorandum NESDIS NGDC-24, National Geophysical Data Center, NOAA, doi:10.7289/V5C8276M.

An, M. *et al.*, 2015. S-velocity model and inferred Moho topography beneath the Antarctic Plate from Rayleigh waves, *J. geophys. Res.,* **120,** 359–383.

Anthony, R.E. *et al.*, 2015. The seismic noise environment of Antarctica, *Seismol. Res. Lett.,* **86,** 89–100.

Ardhuin, F., Stutzmann, E., Schimmel, M. & Mangeney, A., 2011. Ocean wave sources of seismic noise, *J. geophys. Res.,* **116,** C09004, doi:10.1029/2011JC006952.

Ardhuin, F., Balanche, A., Stutzmann, E. & Obrebski, M., 2012. From seismic noise to ocean wave parameters: general methods and validation, *J. geophys. Res.,* **117,** C05002, doi:10.1029/2011JC007449.

Ardhuin, F. & Herbers, T.H.C., 2013. Noise generation in the solid Earth, oceans and atmosphere, from nonlinear interacting surface gravity waves in finite depth, *J. Fluid Mech.,* **716,** 316–348.

Astiz, L., Earle, P.S. & Shearer, P.M., 1996. Global stacking of broadband seismograms, *Seismol. Res. Lett.,* **67**(4), 8–18.

Backus, M., Burg, J., Baldwin, D. & Bryan, E., 1964. Wide-band extraction of mantle *P* waves from ambient noise, *Geophysics,* **29**(5), 672–692.

Benson, G.D., Ritzwoller, M.H., Barmin, M.P., Levshin, A.L., Lin, F-C, Moschetti, M.P., Shapiro, N.M. & Yang, Y., 2007. Processing seismic ambient noise data to obtain reliable broad-band surface wave dispersion measurements, *Geophys. J. Int.,* **169,** 1239–1260.

Beucler, É., Mocquet, A., Schimmel, M., Chevrot, S., Quillard, O., Vergne, J. & Sylvander, M., 2015. Observation of deep water microseisms in the North Atlantic Ocean using tide modulations, *Geophys. Res. Lett.,* **42,** 316–322.

Blankenship, D.D., Anandakrishnan, S., Kempf, J.L. & Bentley, C.R., 1987. Microearthquakes under and alongside Ice Stream B, Antarctica, detected by a new passive seismic array, *Ann. Glaciol.,* **9,** 30–34.

Bromirski, P.D. & Duennebier, F.K., 2002. The near-coastal microseism spectrum: spatial and temporal wave climate relationships, *J. geophys. Res.,* **107,** B82166, doi:10.1029/2001JB000265.

Bromirski, P.D. & Gerstoft, P., 2009. Dominant source regions of the Earth's "hum" are coastal, *Geophys. Res. Lett.,* **36,** L13303, doi:10.1029/2009GL038903.

Bromirski, P.D., Duennebier, F.K. & Stephen, R.A., 2005. Mid-ocean microseisms, *Geochem. Geophys. Geosyst.,* **6**(4), Q04009, doi:10.1029/2004GC000768.

Bromirski, P.D., Stephen, R.A. & Gerstoft, P., 2013. Are deep-ocean-generated surface-wave microseisms observed on land? *J. geophys. Res.,* **118,** 3610–3629.

Burg, J.P., 1964. Three-dimensional filtering with an array of seismometers, *Geophysics* **29**(5), 693–713.

Cavalieri, D.J., Parkinson, C.L., Gloersen, P. & Zwally, H., 1996 (updated yearly). *Sea Ice Concentrations from Nimbus-7 SMMR and DMSP SSM/I-SSMIS Passive Microwave Data*, Digital Media, Boulder, CO, USA: NASA National Snow and Ice Data Center Distributed Active Archive Center. Accessed 7th July 2015.

Cessaro, R.K., 1994. Sources of primary and secondary microseisms, *Bull. seism. Soc. Am.,* **84**(1), 142–148.

Chaput, J. *et al.*, 2014. The crustal thickness of West Antarctica, *J. geophys. Res.,* **119,** doi:10.1002/2013JB010642.

Davy, C., Stutzmann, E., Barruol, G., Fontaine, F.R. & Schimmel, M., 2015. Sources of secondary microseisms in the Indian Ocean, *Geophys. J. Int.,* **202,** 1180–1189.

Euler, G.G., Wiens, D.A. & Nyblade, A.A., 2014. Evidence for bathymetric control on the distribution of body wave microseism sources from temporary seismic arrays in Africa, *Geophys. J. Int.*, doi:10.1093/gji/ggu105.

Gal, M., Reading, A.M., Ellingsen, S.P., Gualtieri, L., Koper, K.D., Burlacu, R., Tkalčić, H. & Hermer, M.A., 2015. The frequency dependence and locations of short-period microseisms generated in the Southern Ocean and West Pacific, *J. geophys. Res.,* **120,** 5764–5781.

Gerstoft, P., Fehler, M.C. & Sabra, K.G., 2006a. When Katrina hit California, *Geophys. Res. Lett.,* **33,** L17308, doi:10.1029/2006GL027270.

Gerstoft, P., Sabra, K.G., Roux, P., Kuperman, W.A. & Fehler, M.C., 2006b. Green's function extraction and surface-wave tomography from microseisms in southern California, *Geophysics,* **71**(4), SI23–SI31.

Gerstoft, P., Shearer, P.M., Harmon, N. & Zhang, J., 2008. Global P, PP, and PKP wave microseisms observed from distant storms, *Geophys. Res. Lett.,* **35,** L23306, doi:10.1029/2008GL036111.

Grob, M., Maggi, A. & Stutzmann, E., 2011. Observations of the seasonality of the Antarctic microseismic signal, and its association to sea ice variability, *Geophys. Res. Lett.,* **38,** L11302, doi:10.1029/2011GL047525.

Gualtieri, L., Stutzmann, E., Capdeville, Y., Ardhuin, F., Schimmel, M., Mangeney, A. & Morelli, A., 2013. Modeling secondary microseismic noise by normal mode summation, *Geophys. J. Int.,* **193,** 1732–1745.

Gualtieri, L., Stutzmann, E., Capdeville, Y., Farra, V., Mangeney, A. & Morelli, A., 2015. On the shaping factors of the secondary microseismic wavefield, *J. geophys. Res.,* **120,** doi:10.1002/2015JB012157.

Hasselmann, K., 1963. A statistical analysis of the generation of microseisms, *Rev. Geophys.,* **1**(2), 177–210.

Haubrich, R.A., 1968. Array design, *Bull. seism. Soc. Am.,* **58**(3), 977–991.

Haubrich, R.A., Munk, W.H. & Snodgrass, F.E., 1963. Comparative spectra of microseisms and swell, *Bull. seism. Soc. Am.,* **53**(1), 27–37.

Haubrich, R.A. & McCamy, K., 1969. Microseisms: coastal and pelagic sources, *Rev. Geophys.,* **7**(3), 539–571.

Heeszel, D.S., Wiens, D.A., Nyblade, A.A., Hansen, S.E., Kanao, M., An, M. & Zhao, Y., 2013. Rayleigh wave constraints on the structure and tectonic history of the Gamburtsev Subglacial Mountains, East Antarctica, *J. geophys. Res.,* **118,** 2138–2153.

Kværna, T., 1989. On exploitation of small-aperture NORESS type arrays for enhanced *P*-wave detectability, *Bull. seism. Soc. Am.,* **79,** 888–900.

Kedar, S., 2011. Source distribution of ocean microseisms and implications for time-dependent noise tomography, *C. R. Geosci.,* **343,** 548–547.
Kedar, S., Longuet-Higgins, M., Webb, F., Graham, N., Clayton, R. & Jones, C., 2008. The origin of deep ocean microseisms in the North Atlantic Ocean, *Proc. R. Soc. A.,* **464,** 777–793.
Kennett, B.L.N., 1986. *Lg* waves and structural boundaries, *Bull. seism. Soc. Am.,* **76,** 1133–1141.
Kennett, B.L.N., Engdahl, R.E. & Buland, R., 1995. Constraints on seismic velocities in the Earth from travel times, *Geophys. J. Int.,* **122,** 108–124.
Koch, F.W., Wiens, D.A., Euler, G.G., Nyblade, A.A., Anandakrishnan, S., Huerta, A., Wilson, T.J. & Aster, R.C., 2013. Tracking the effect of sea ice cover on microseismic noise using two seismic arrays in Antarctica, in *Abstract Seismological Society of America Annual Meeting*, Salt Lake City, Utah, 17–19 April 2013.
Koper, K.D. & Burlacu, R., 2015. The fine structure of double-frequency microseisms recorded by seismometers in North America, *J. geophys. Res.,* **120,** 1677–1691.
Koper, K.D., de Foy, B. & Benz, H.M., 2009. Composition and variation of noise recorded at the Yellowknife seismic array, 1991–2007, *J. geophys. Res.,* **114,** B10310, doi:10.1029/2009JB006307.
Koper, K.D., Seats, K. & Benz, H.M., 2010. On the composition of Earth's short period seismic noise field, *Bull. seism. Soc. Am.,* **100**(2), 606–617.
Landès, M., Hubans, F., Shapiro, N.M., Paul, A. & Campillo, M., 2010. Origin of deep ocean microseisms by using teleseismic body waves, *J. geophys. Res.,* **115,** B05302, doi:10.1029/2009JB006918.
Larose, E., Derode, A., Clorennec, D., Margerin, L. & Campillo, M., 2005. Passive retrieval of Rayleigh waves in disordered elastic media, *Phys. Rev. E.,* **72,** doi:10.1103/PhysRevE.72.046607.
Lawrence, J.F., Wiens, D.A., Nyblade, A.A., Anandakrishnan, S., Shore, P.J. & Voigt, D., 2006. Rayleigh wave phase velocity analysis of the Ross Sea, Transantarctic Mountains, and East Antarctica from a temporary seismograph array, *J. geophys. Res.,* **111,** B06302, doi:10.1029/2005JB003812.
Liu, Q. *et al.*, 2016. Source locations of teleseismic P, SV, and SH waves observed in microseisms recorded by a large aperture seismic array in China, *Earth planet. Sci. Lett.,* **449,** 39–47.
Longuet-Higgins, M.S., 1950. A theory of the origin of microseisms, *Phil. Trans. R. Soc. Lond., A,* **243**(857), 1–35.
Obrebski, M., Ardhuin, F., Stutzmann, E. & Schimmel, M., 2013. Detection of microseismic compressional (*P*) body waves aided by numerical modeling of oceanic noise sources, *J. geophys. Res.,* **118,** 4312–4324.
Pratt, M.J., Winberry, J.P., Wiens, D.A., Anandakrishnan, S. & Alley, R.B., 2014. Seismic and geodetic evidence for grounding-line control of Whillans Ice Stream stick–slip events, *J. geophys. Res.,* **119,** 333–348.
Pyle, M., Wiens, D.A., Nyblade, A.A. & Anandakrishnan, S., 2010. Crustal structure of the Transantarctic Mountains near the Ross Sea from ambient seismic noise tomography, *J. geophys. Res.,* **115,** B11310, doi:10.1029/2009JB007081.
Reading, A.M., Koper, K.D., Gal, M., Graham, L.S., Tkalčić, H. & Hemer, M.A., 2014. Dominant seismic noise sources in the Southern Ocean and West Pacific, 2000–2012, recorded at the Warramunga Seismic Array, Australia, *Geophys. Res. Lett.,* **41,** 3455–3463.
Rost, S. & Thomas, C., 2002. Array seismology: methods and applications, *Rev. Geophys.,* **40**(3), 1008–1034.
Rost, S. & Thomas, C., 2009. Improving seismic resolution through array processing techniques, *Surv. Geophys.,* **30,** 271–299.
Rowe, C., Aster, R.C., Kyle, P.R. & Schlue, J.W., 1998. Broadband recording of Strombolian explosions and associated very-long-period seismic signals on Mount Erebus volcano, Ross Island, Antarctica, *Geophys. Res. Lett.,* **25**(13), 2297–2300.
Shapiro, N.M. & Campillo, M., 2004. Emergence of broadband Rayleigh waves from correlations of the ambient seismic noise, *Geophys. Res. Lett.,* **31,** doi:10.1029/2004GL019491.
Simmonds, I., 2015. Comparing and contrasting behaviour of Arctic and Antarctic sea ice over the 35 year period 1978–2013, *Ann. Glaciol.,* **56**(69), doi:10.3189/2015AoG69A909.
Stutzmann, E., Ardhuin, F., Schimmel, M., Mangeney, A. & Patau, G., 2012. Modelling long-term seismic noise in various environments, *Geophys. J. Int.,* **191,** 717–722.
Tolman, H.L., 2009. User manual and system documentation of WAVEWATCH III version 3.14. *NOAA/NWS/NCP/MMAB Technical Note 276.*
Tournadre, J., Whitmer, K. & Girard-Ardhuin, F., 2008. Iceberg detection in open water by altimeter waveform analysis, *J. geophys. Res.,* **113,** doi:10.1029/2007JC004587.
Traer, J., Gerstoft, P., Bromirski, P.D. & Shearer, P.M., 2012. Microseisms and hum from ocean surface gravity waves, *J. geophys. Res.,* **117,** B11307, doi:10.1029/2012JB009550.
Tsai, V.C. & McNamara, D.E., 2011. Quantifying the influence of sea ice on ocean microseism using observations from the Bering Sea, Alaska, *Geophys. Res. Lett.,* **38,** doi:10.1029/2011GL049791.
Vinnik, L.P., 1973. Sources of microseismic *P* waves, *Pure appl. Geophys.,* **103,** 282–289.
Weaver, R.L. & Lobkis, O.I., 2001a. Ultrasonics without a source: thermal fluctuation correlation at MHz frequencies, *Phys. Rev. Lett.,* **87**(13), 134301, doi:10.1103/PhysRevLett.87.134301.
Weaver, R.L. & Lobkis, O.I., 2001b. On the emergence of the Green's function in the correlations of a diffuse field, *J. acoust. Soc. Am.,* **110,** 3011–3017.
Webb, S.C., 1998. Broadband seismology and noise under the ocean, *Rev. Geophys.,* **36,** 105–142.
Winberry, J.P., Anandakrishnan, S., Wiens, D.A. & Alley, R.B., 2013. Nucleation and seismic tremor associated with the glacial earthquakes of Whillans Ice Stream, Antarctica, *Geophys. Res. Lett.,* **40,** 312–315.
Winberry, J.P., Anandakrishnan, S., Alley, R.B., Wiens, D.A. & Pratt, M.J., 2014. Tidal pacing, skipped slips and the slowdown of the Whillans Ice Stream, Antarctica, *J. Glaciol.,* **60,** 795–807.
Zhang, J., Gerstoft, P. & Bromirski, P.D., 2010. Pelagic and coastal sources of *P*-wave microseisms: generation under tropical cyclones, *Geophys. Res. Lett.,* **37,** L15301, doi:10.1029/2010GL044288.

SUPPORTING INFORMATION

Supplementary data are available at *GJIRAS* online.

1 Power spectral density analysis of POLENET stations and the WIS Array

Figure S1.1. PSD variations over a 2 yr interval at POLENET/ANET stations MPAT and SURP (locations shown in Fig. 1a). Daily PSDs are created using the median of 3 hr windows. Amplitudes are shown in dB relative to $10\log_{10}$ m^2 s^{-4} Hz^{-1}. SF, LPDF and SPDF microseisms are separated by dashed lines. The red box denotes the time period of the WIS Array. Peak amplitudes are observed during the latter portion of austral summer (January–April) when sea ice is at a minimum. A comparison of these spectrograms to WIS Array station BB01 is shown in Fig. S2.5.
Figure S1.2. Averaged power spectral density (PSD) functions of the WIS Array for 2010 December 13th–16th and 2011 January 26th–29th and average PSD for MPAT and SURP for 13th December–29th January (orange solid and dashed lines respectively). Dashed lines mark the global IDC2010 noise model of Brown *et al*. (2014) as reference of global high and low noise levels. SF, LPDF, SPDF and USPDF microseism bands as marked by grey bars. Note the increase (arrow) in power in the SF microseism band at the end of January relative to the start of December, which correlates with the reduction in Antarctic sea ice extent.

2 Additional Table and Figures

Table S2.1. Seismic stations used.
Figure S2.1. Adapted from Gerstoft *et al*. (2008), (a) slowness–distance graph of body wave phases of strong amplitude (Astiz *et al*. 1996) using reference model AK135 (Kennett *et al*. 1995). Note that more than one phase can have the same slowness (dashed

line) leading to ambiguity in epicentral distance to the wave source when back projecting. (b) Example paths of body wave mantle phases (*P* and *PP*) and core phases (*PKP*) from sources to receiver. Colours are the same in both plots.

Figure S2.2. Rayleigh wave excitation coefficients ($m = 1$–4 in eq. 4) for wave–wave interactions calculated from values given by Longuet-Higgins (1950) for 6 and 10 s, respectively. The excitation function is a function of bathymetry with shorter periods exciting microseisms at shallower ocean depths. Excitation of LPDF microseisms occurs over a much larger area, whereas SPDF microseism excitation is confined to continental slopes and shallower sea mounts. Ice extent and WIS Array shown as in Fig. 1(a).

Figure S2.3. Variation of the modelled noise spectrum due to the attenuation parameter at 6 and 10 s throughout January 2011 at station BB01. Blue lines represent the daily observed power at station BB01. (a) and (c) show the model results when reflections from icebergs and small islands and not included; (b) and (d) show results from a model where reflection coefficients are set to 40 per cent for icebergs, 20 per cent for small islands and 10 per cent for coastlines. The Q value range is set to reasonable values explored by other studies (Stutzmann *et al*. 2012).

Figure S2.4. SF, LPDF and SPDF power as recorded at MPAT and SURP over the same duration as Fig. S1.1. Each day is plotted as a black point and a smoothing spline has been drawn to help show the significant annual variation. Peaks in SF and SPDF energy correlate with the variations in sea ice concentration as shown with coloured vertical lines corresponding to the concentration maps above. The red and tan stars mark the locations of MPAT and SURP respectively. Note the vertical scale changes to highlight peaks in the data and the much larger spread of values for the LPDF band.

Figure S2.5. Comparison of spectrograms between the two POLENET stations and BB01 in the WIS Array. Site variations may be a factor in the variations between SURP which was deployed on bedrock, and BB01which was buried 50 cm into the firn layer.

Figure S2.6. (a) Direction of SF beam power with slowness of 27–40 s deg^{-1} for December 2010 and January 2011. The December map shows two distinct source regions in the direction of the Antarctic Peninsula and George V Land. The January map shows the addition of the third source from Dronning-Maude Land, grid north of the array centre, as well as the strengthening of the George V Land source relative to the Antarctic Peninsula. (b) For the LPDF band at 27–40 s deg^{-1}. The directional pattern shows a strengthening of LPDF microseism power from most other directions relative to the Antarctic Peninsula source. (c) For the SPDF band at 20–35 s deg^{-1} which predominantly covers the interpreted *Lg* slownesses.

Figure S2.7. Sea ice concentration variations in Dronning-Maude Land throughout the course of the WIS Array deployment. Significant sea ice loss by January 3rd 2011 allows swells to reach the continental shelf in the region producing strong SF microseism energy. Bathymetry from ETOPO1.

Figure S2.8. Modelled source locations for 2010 December 30th using the *P*-wave excitation for comparison with Fig. 8(c). Source locations are similar between this map and that shown for the Rayleigh wave excitation.

Figure S2.9. Bathymetric excitation coefficient as a function of depth for different frequencies of Rayleigh and *P* waves. Note that the maximum peak for the LPDF and SPDF period bands lie at roughly the same depths for both phases. Bathymetry used is the Global05 included in WW3: 0.5° resolution between 80°N and 78°S. Rayleigh wave group velocity is set as constant at 3 km s^{-1} and sedimentary basins are not included in our model runs.

Figure S2.10. Monthly *f*–*s* maps at 0.33–2 s, ranging from 0 to 15 s deg^{-1}, showing body wave arrivals at *P*+*PP* and *PKPbc* slownesses. Numbers on the December map refer to the same locations shown on Fig. 10—1: Peter I Island–South Chile, 2: Scotia, 3: Cape of Good Hope, 4: Conrad Rise, 5: North Kerguelen Plateau, 6: South Kerguelen Plateau, 7: West Australia, 8: Great Australian Bight, 9: Vanuatu earthquakes, 10: Tonga earthquakes, 11: Southern Greenland.

3 Movies

Movie 1. 10s_model_with_seismic_REF.mp4
Movie 2. 6s_model_with_seismic_REF.mp4
Movie 3. 0.3-2s_backprojected.mp4